Supporting Information

Contactless near-field scanning thermoreflectance imaging

Sabastine Ezugwu,[a,†] Sina Kazemian,[a,†] Dong-Yup William Choi,[a] and Giovanni Fanchini[a,b,*]

[a] *Department of Physics & Astronomy, University of Western Ontario, London, ON, N6A 3K7, Canada.*
[b] *Department of Chemistry, University of Western Ontario, London, ON, N6A 5B7, Canada.*
† These authors contributed equally to this work.

Table of Contents

1) Linear relationship between thermoreflectance amplitude and surface temperature

1a – Reflectance due to light scattering at the tip aperture

Here, we offer a proof of the existence of a direct proportionality between the amplitude of the thermoreflectance signal $\delta\rho_0(x,y)$, measured by near-field scanning thermoreflectance imaging (NeSTRI), and $T_0(x,y)$, the temperature at the sample surface, which is expressed by eq. 6 in our paper. Validity of eq. 6 is essential to infer $T_0(x,y)$ from NeSTRI measurements. In our proof, we will assume the validity of Rayleigh's assumptions [s1] for electromagnetic radiation scattered at the aperture of the scanning near-field optical microscope (SNOM) tip. Rayleigh's law is valid for scattering by objects with individual dimensions that are small compared with the wavelength of incident radiation. We assume that incident oscillating electric and magnetic fields induce electric and magnetic multipoles at the boundaries of the tip aperture, which oscillate in phase with the incident electromagnetic wave, and radiate energy in different directions. Furthermore, the tip apertures used in our SNOM and NeSTRI experiments are coated with non-ferromagnetic metals, in which electric dipoles are more significant than magnetic dipoles, so our proof will only deal with electric dipoles. As far as the wavelength is long compared to the size of the aperture, only multipoles of the lowest order, electric dipoles, are important.

The geometry we utilize for our proof, which is a good approximation of our experimental setup, is shown in Figure S1. Incident radiation is a plane monochromatic wave at wavenumber *k* and wavelength $\lambda = 2\pi/k$, with direction of incidence defined by the unit vector $\mathbf{n_0}$, and complex incident polarization vector $\mathbf{e_0}$. It impinges an aperture of radius a bored in a relatively flat SNOM cantilever of thickness L. The associated incident electric field of intensity E_0 can be expressed as

$$E_{inc} = \mathbf{e_0} E_0 e^{ik\mathbf{n_0}\cdot x} . \tag{S1}$$

E_{inc} induces electric dipoles moments $\boldsymbol{p}$ and magnetic dipole moments $\boldsymbol{\mu}$ on the cylindrical surface of the SNOM tip aperture, which acts as a scatterer. Dipoles radiate energy at any generic directions indicated by unit vectors **n** and polarization vectors **e**. Far away from the aperture, the intensity of the scattered field along a generic direction is given by [s1]

$$E_{sc}^{(\mathbf{n})} = \frac{1}{4\pi\varepsilon_0} k^2 \frac{e^{ikr}}{r} \left[(\mathbf{n} \times \boldsymbol{p}) \times \mathbf{n} - \mathbf{n} \times \boldsymbol{\mu} / c \right] \approx \frac{1}{4\pi\varepsilon_0} k^2 \frac{e^{ikr}}{r} (\mathbf{n} \times \boldsymbol{p}) \times \mathbf{n} \,, \qquad \text{(S2)}$$

where r is the distance between the tip aperture and the observer, c is the speed of light and ε_0 is the dielectric permittivity in air, which is relatively close to that of vacuum. We neglect the second addend in eq. S2 since our SNOM tips are non-ferromagnetic and $|\boldsymbol{\mu}|/c << |\boldsymbol{p}|$.

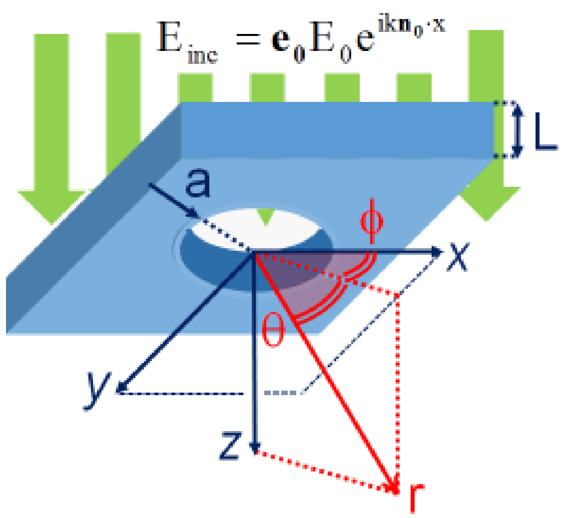

Figure S1. *Small circular SNOM tip aperture of radius* a *and thikness* L *(*a *and* L $<< \lambda = k/2\pi$*) drilled in a dielectric and non-ferromagnetic material and acting as a scatterer for plane and incident electromagnetic waves. The observer is positioned at a distance* r *and angle* θ *from the aperture.*

Because the intensity of electromagnetic radiation is proportional to the square of the electric field, the amount of reflected light at any given direction is given by

$$\rho^{(\mathbf{n})} = \frac{\left|E_{sc}^{(\mathbf{n})}\right|^2}{\left|E_{inc}\right|^2} \tag{S3}$$

To calculate the reflectance, the scattered and incident electric fields given by eqs. S2 and S1 must be replaced into eq. S3. In addition, it must be considered that the magnitude of the electric dipoles at the surface depend on the intensity of the incident electric field. Thus $|\boldsymbol{p}| \sim E_0$, with a proportionality coefficient that also depends on the complex dielectric constant (or complex refractive index) of the tip material. Finally, scattering contributions at point r from all of the induced electrical dipoles at the scatterer surface must be superimposed by means of an integration. For solving this scattering problem in an arbitrary geometry, it is convenient to decompose the two field vectors into components that are, respectively, parallel ($E_{//sc}^{(n)}$ and $E_{//inc}$) and perpendicular ($E_{\perp sc}^{(n)}$ and $E_{\perp inc}$) to $\mathbf{n_0}$, and write them in a matrix form [s2]. Eq. S2 can thus be generalized as

$$\begin{bmatrix} E_{//sc}^{(\mathbf{n})} \\ E_{\perp sc}^{(\mathbf{n})} \end{bmatrix} = \frac{e^{ik(r-z)}}{-ikr} \cdot \mathbf{S} \cdot \begin{bmatrix} E_{//inc} \\ E_{\perp inc} \end{bmatrix}. \tag{S4}$$

In our particular cylindrical geometry, **S**, the scattering matrix, can be expressed as [s2]

$$\mathbf{S} = \frac{3ik^3}{4\pi} \cdot \left|\frac{m^2-1}{m^2+2}\right| \cdot V \cdot f(\theta,\phi) \cdot \begin{bmatrix} \cos\theta & 0 \\ 0 & 1 \end{bmatrix}. \tag{S5}$$

This expression depends on the volume of the cylindrical aperture, $V = \pi a^2 L$, and on the form factor f, which is a consequence of the superimposition of the contributions from all of the dielectric dipoles in the particular geometry under consideration. For a cylinder, the form factor can be calculated as

$$f(\theta,\phi)=\frac{1}{\pi La^{2}}\int_{-\frac{L}{2}}^{\frac{L}{2}}dz\int_{0}^{2\pi}d\phi\int_{0}^{a}dr\cdot r\cdot\exp\left(\frac{2\pi i}{L}r\cos\theta\right), \tag{S6}$$

from which it can be seen that $f(\theta,\phi) \approx -2$ in the long wavelength approximation, at $a << \lambda$. Equation S5 also depends on the complex refractive indices of the two media, air and the tip material, through the factor $|(m^2 - 1) / (m^2 + 2)|$ that is reminiscent of the proportionality factor between $\boldsymbol{p}$ and E_0 offered by Clausius-Mossotti relationship. [s3] Also, in eq. (S5) m is the optical contrast coefficient

$$m=\frac{M_a}{M_t}\approx\frac{N_a}{N_t+iK_t} \tag{S7}$$

that represents the ratio between the complex refractive index of the tip material ($M_t = N_t+iK_t$) and air, for which $M_a \approx N_a \sim 1$. In the specific geometry used for NeSTRI and SNOM measurements, the SMA coupler used to collect the reflected light is placed at the same z-axis level of the tip and therefore, at $\theta = 90^o$. In these conditions, and for $f(\theta,\phi) \approx -2$, eqs. S4 and S5 lead to the relationship

$$E_{sc}{}^{2}=\frac{3}{2}\left|\frac{m^{2}-1}{m^{2}+2}\right|L^{2}a^{4}\frac{e^{2ikr}}{r^{2}}k^{4}E_{inc}{}^{2}, \tag{S8}$$

and, for $\langle\exp(2ikr)\rangle \approx ½$, to the following expression of the reflectance at $\theta = 90^o$:

$$\rho=12\pi^{4}\frac{L^{2}a^{4}}{r^{2}\lambda^{4}}\cdot\left|\frac{m^{2}-1}{m^{2}+2}\right|. \tag{S9}$$

The λ^4 dependence of eq. S9 on the wavelength of the probe beam is reminiscent of a similar dependence in Rayleigh scattering [s1], and is indicative of the fact that Rayleigh's law and eq. S9 are derived under the same assumptions.

2a – Amplitude of the thermoreflectance signal

In thermoreflectance measurements, the reflection coefficient determined via eq. S9 changes with the temperature of air due to the temperature dependence of m. When light heats the sample, heat is transferred to air that decreases in density, and its refractive index decreases accordingly, as

$$N_a(T) = N_a(0) - \chi T \tag{S10}$$

where $N_a(0) \approx 1$ is the refractive index of air under ambient conditions, in the absence of transferred heat, and $\chi \approx 6\ 10^{-4}\ K^{-1}$ is the air thermo-optical coefficient. [s4] It is worthwhile noting that, although χ is quite small, it has been demonstrated by several experiments in the literature to be sufficient to perform thermoreflectance measurements at the microscopic levels even with powers that are significantly lower than those used in our experiments [s5]. In order to estimate how eq. S10 affects the reflectance determined via eq. S9, we consider that $N_t^2 << K_t^2$ for nontransparent tip materials such as, in our experiments, aluminum (for which $M_t = N_t + iK_t = 0.90 + i6.21$ at λ = 532 nm probe beam wavelength [s6]). Thus, we can write

$$m(T)^2 \approx \frac{\left(N_a(0) - \chi T\right)^2}{\left(N_t + iK_t\right)^2} \approx -\frac{1 - 2\chi T}{K_t^{\,2}}. \tag{S11}$$

From this expression, by expanding the Clausius-Mossotti factor in Taylor series for sufficiently small values of m [i.e. $(m^2 - 1) / (m^2 + 2) \approx -\frac{1}{2} + \frac{3}{4} m^2$] and by substituting it into eq. S9, we obtain the following expression for the temperature-dependent reflectance at the tip-air interface:

$$\rho(T) = \rho(0) + \delta\rho(T) \approx 12\pi^4 \frac{L^2 a^4}{r^2 \lambda^4}\left(\frac{1}{2} - \frac{2\chi}{K_t^{\,2}} T\right). \tag{S12}$$

It is thus demonstrated that, under our specific assumptions, the thermoreflectance at the sample surface is given by

$$\delta\rho_0(x,y) \approx -24\pi^4 \frac{L^2 a^4}{r^2 \lambda^4} \frac{\chi}{K_t^{\ 2}} T_0(x,y). \tag{S13}$$

Thus, from our derivation, the proportionality coefficient between $\delta\rho_0(x,y)$ and $T_0(x,y)$, which we introduced in equation 9, can be estimated as

$$h = -24\pi^4 L^2 a^4 \chi \,/\, (r^2 \lambda^4 K_t^2). \tag{S14}$$

In eq. S14, h does not depend on the specific location of the sample at which the thermoreflectance is measured. It only depends on the radius and length of the tip aperture, the optical properties of the system, the probe beam wavelength, and the distance between the sample and the detector. Consequently, due to the generality of our derivation which does not assume any significant tip-sample interaction, it remains demonstrated that the amplitude of the thermoreflectance signal measured by NeSTRI is linearly proportional to the temperature at the sample surface. It is worthwhile noting, from eq. (S14), that $h < 0$. Consequently, the thermoreflectance is lower at the times and locations at which the temperature is locally higher and the phases of $T_0(x,y)$ and $\delta\rho_0(x,y)$ are shifted by 180°. Therefore, the two quantities are in phase opposition.

2) Finite-difference method used to generate thermal conductivity images from equation 8

2.1 Formulation of equation 9 in terms of finite differences

In this section, we develop a numerical algorithm capable of modelling, from phase [$\delta\varphi_0(x,y)$] and amplitude [$\delta\rho_0(x,y)$] thermoreflectance images, the diffusion of heat along an inhomogeneous thermally conducting thin film on a thermally insulating substrate. Objective of the algorithm is to reconstruct, from thermoreflectance phase and amplitude images, the thermal conductivity $k(x,y)$ that inhomogeneously varies from point to point of the film. Equation 8 in the text is written as

$$\begin{aligned} &\nabla k(x,y)\cdot\nabla\delta\rho_0(x,y)+k(x,y)\nabla^2\delta\rho_0(x,y)-k(x,y)\delta\rho_0(x,y)[\nabla\delta\varphi_0(x,y)]^2 \\ &= hP_0A_0(x,y)\cos[\delta\varphi_0(x,y)] \end{aligned}. \tag{S15}$$

Eq. S15 represents the real part of Fourier equation for periodic and inhomogeneous heat generation in a sample of optical absorbance $A_0(x,y)$. A pump laser at uniform power density P_0 impinges the imaged sample area, and heat is locally generated proportionally to the amount of power being locally absorbed by the thin film. In our experiments, the substrate is optically non-absorbing. Both P_0 and $A_0(x,y)$ are known from independent experiments. The thermal conductivity $k(x,y)$ is unknown, and so is h, the proportionality coefficient given by eq. S14 that is independent of x and y. Due to the arbitrary and nonanalytical nature of $A_0(x,y$, $\delta\varphi_0(x,y)$ and $\delta\rho_0(x,y)$, eq. S15 is a 2D first-order equation in $k(x,y)$ which needs to be solved numerically.

To solve eq. S15, we here introduce a first-order, finite-difference method, in which the differential equation of an image of P×Q pixels, will be transformed in an algebraic system of P×Q linear equations in the same number of scalar unknowns. We write eq. S15 in a way that each differential term, known or unknown, is expressed by a finite difference (FD). The following known FD terms are calculated (for i = 1…P and j = 1… Q) from the thermoreflectance amplitude image [$\delta\rho_0(i,j)$]:

$$\nabla\delta\rho_0(x,y) \approx \mathrm{U}_{\mathrm{i,j}}\hat{\mathbf{i}} + \mathrm{V}_{\mathrm{i,j}}\hat{\mathbf{j}} = \frac{\delta\rho_0(i\pm 1,j)\text{-}\delta\rho_0(i,j)}{\delta x}\hat{\mathbf{i}} + \frac{\delta\rho_0(i,j\pm 1)\text{-}\delta\rho_0(i,j)}{\delta y}\hat{\mathbf{j}}, \tag{S16}$$

$$\nabla^2\delta\rho_0(x,y) \approx \frac{\mathrm{U}_{\mathrm{i\pm1,j}}\text{-}\mathrm{U}_{\mathrm{i,j}}}{\delta x} + \frac{\mathrm{V}_{\mathrm{i,j\pm1}}\text{-}\mathrm{V}_{\mathrm{i,j}}}{\delta y}, \tag{S17}$$

where $U_{i,j}$ and $V_{i,j}$ are the two scalar components of the thermoreflectance gradient and **i** and **j** represent two unit vectors along coordinate directions x and y, respectively. The following known FD term is calculated from both the thermoreflectance phase [$\delta\varphi_0(i,j)$] and amplitude images:

$$\delta\rho_0(x,y)\left[\nabla\delta\varphi_0(x,y)\right]^2 \approx \mathrm{Z}_{\mathrm{i,j}} = \delta\rho_0(i,j)\left\{\frac{\left[\delta\varphi_0(i\pm 1,j)\text{-}\delta\varphi_0(i,j)\right]^2}{\delta x^2} + \frac{\left[\delta\varphi_0(i,j\pm 1)\text{-}\delta\varphi_0(i,j)\right]^2}{\delta y^2}\right\}. \tag{S18}$$

In eqs. S16-S19, δx and δy are the width and height of each pixel, which are independent of i and j. In addition, in eq. S15, the unknown term $\nabla k(x,y)$ is written as a finite difference in the form:

$$\nabla k(x,y) \approx \frac{k_{\mathrm{i\pm1,j}} - k_{\mathrm{i,j}}}{\delta x}\hat{\mathbf{i}} + \frac{k_{\mathrm{i,j\pm1}} - k_{\mathrm{i,j}}}{\delta y}\hat{\mathbf{j}}. \tag{S19}$$

where $k(x,y) \approx k_{i,j}$ at any point (i,j). The FDs expressed by eqs. S16-S19 can be replaced into eq. S16 to obtain a set of algebraic finite-difference equations of the form

$$\mathrm{X}_{\mathrm{i,j}} \cdot K_{\mathrm{i\pm1,j}} + \mathrm{Y}_{\mathrm{i,j}} \cdot K_{\mathrm{i,j\pm1}} + \mathrm{H}_{\mathrm{ij}} \cdot K_{\mathrm{i,j}} = \mathrm{G}_{\mathrm{i,j}}, \tag{S20}$$

in which the following quantities have been defined for compactness:

$$\begin{aligned}
&\mathrm{X}_{\mathrm{i,j}} = \mathrm{U}_{\mathrm{i,j}}/\delta x \\
&\mathrm{Y}_{\mathrm{i,j}} = \mathrm{V}_{\mathrm{i,j}}/\delta y \\
&\mathrm{H}_{\mathrm{i,j}} = \mathrm{X}_{\mathrm{i\pm1,j}} - 2\mathrm{X}_{\mathrm{i,j}} + \mathrm{Y}_{\mathrm{i,j\pm1}} - 2\mathrm{Y}_{\mathrm{i,j}} - \mathrm{Z}_{\mathrm{ij}}/\mathrm{h}\,. \\
&\mathrm{G}_{i,j} = P_0 \cdot A_0(x,y) \cdot cos\left[\delta\varphi_0(i,j)\right] \\
&K_{\mathrm{i,j}} = (k_{\mathrm{i,j}} - k_{\mathrm{G}})/h
\end{aligned} \tag{S21}$$

Where k_G is the thermal conductivity of the substrate (i.e. $k = k_G = 1.1$ W/m/K in the case of glass). In total, a number of P×Q scalar equations of the form of eq. S20 can be written to form an algebraic system in the set of unknowns $\{K_{i,j}\}$ which will be numerically solved, giving us a quantity proportional to thermal conductivity along the surface for each point, with a proportionality constant, *h*, to be determined.

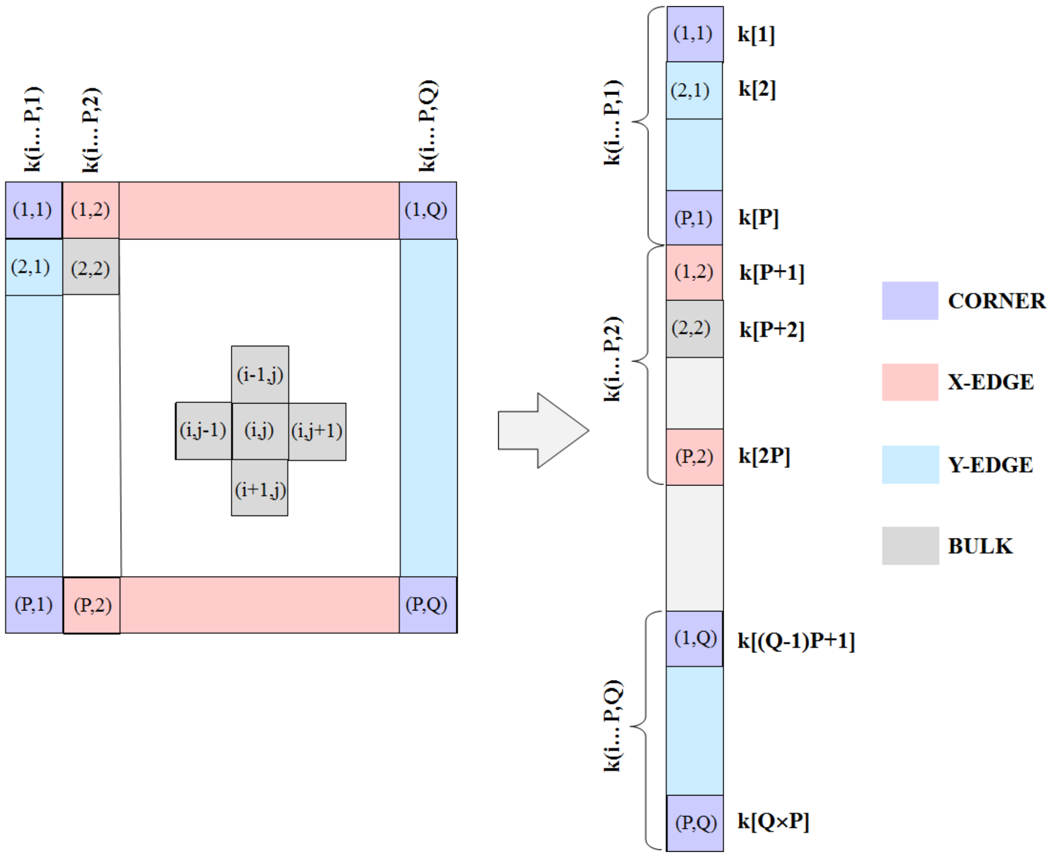

Figure S2. *Scheme used in our numerical finite-difference calculations to transform pixel images* ***K*(j = 1…P, j=1…Q)** *into column vectors* ***K*[1,..., P×Q]**. *These scheme allows us to transform our finite-difference equation, eq. (S22), into an algebraic system of* P×Q *scalar equations in* P×Q *unknowns of the type* **A**·***K*** = **B**, *eq. (S28). Each scalar unknown,* *K*[1], …, *K*[P×Q], *represents the thermal conductivity of a specific pixel* (i,j). *The scalar equations have a different formulation depending if the pixel sits at the corner of the image, at an x-edge, at a y-edge, or in the bulk of the image, which is a consequence of the fact that we impose the boundary condition* **K[b]** = k_G *for any point at an edge, or corner.*

2.2 Solution of the finite-difference system with appropriate boundary conditions

It is important to bear in mind that, although eq. S20 is valid in general, for any pixel (i,j) of our images, the thermal conductivity at the boundaries (i.e. at points where $i = 1$ or P, or $j = 1$ or Q) is known and must be equal to the thermal conductivity of the substrate. Due to the linear character of Fourier's equation S15, for which the principle of superposition is valid, if we solve a system of equations of the form S20 with boundary conditions

$$K_G = K(i = 1 \text{ or } \mathrm{P}, j) = K(i, j = 1 \text{ or } \mathrm{Q}) = 0, \tag{S22}$$

the thermal conductivity at the sample surface will be determined as

$$k_{i,j} = h \cdot K_{i,j} + k_G. \tag{S23}$$

Consequently, our method is fully capable to reconstruct thermal conductivity images $\{k_{i,j}\}$ from NeSTRI experiments.

In order to solve our algebraic system, it is convenient to rearrange it by labelling the variables with a single index, $l = 1,.., \mathrm{P}{\times}\mathrm{Q}$, in lieu of two of them, i and j. The scheme used for such a rearrangement is reported in Figure S2. Each column j forming the images of the known quantities $\mathrm{X}_{i,j}$, $\mathrm{Y}_{i,j}$, $\mathrm{H}_{i,j}$, and $\mathrm{G}_{i,j}$, and of the unknown $K_{i,j}$ is piled in a column vector of P×Q elements. This implies that for a certain number of equations of the form S20 (specifically at $l = 1,\ldots \mathrm{P}$; $l = \mathrm{P}{\times}(\mathrm{Q}-1), \ldots, \mathrm{P}{\times}\mathrm{Q}$; $l = j\mathrm{P}$; and $l = j\mathrm{P}+1$) at least one of the addends at the left hand of equation S20 corresponds to a boundary condition, for which $K_l = K_G = 0$, and is therefore null. In the specific cases of l pointing to image corners, two of the addends at the left hand of equation S20 correspond to boundary conditions and are null. We are dealing with four different types of finite-difference equations of the form S20, depending on the number of boundary conditions they involve:

a) Corner equations correspond to pixels $(i, j) = (1,1)$; $(i, j) = (P, 1)$; $(i, j) = (1, Q)$ and $(i, j) = (P, Q)$ [for which $l = 1$, $l = P$, $l = (Q-1)\times P+1$, and $l = P\times Q$) if a single-index notation is used, as in Figure S2]. In these cases, we have both $K_{i\pm1,j} = K_G = 0$ and $K_{i,j\pm1} = K_G = 0$. By transferring the known terms to the right hand of eq. S20, we obtain four linear equations of the form

$$\mathrm{H}_{\mathrm{ij}} \cdot K_{i,j} = \mathrm{G}_{\mathrm{i,j}} - \mathrm{X}_{\mathrm{i,j}} \cdot K_{\mathrm{G}} - \mathrm{Y}_{\mathrm{i,j}} \cdot K_{\mathrm{G}} = \mathrm{G}_{\mathrm{i,j}}. \tag{S24}$$

b) x-edge equations correspond to pixels $(i, 1)$ and (i, Q) with $i = 2,\ldots, P-1$ [for which $l = jP$ or $l = jP+1$, with $j = 2, \ldots Q-1$) if a single-index notation is used, as in Figure S2]. In these cases, we have $K_{i\pm1,j} = K_G = 0$. By moving the known term $\mathrm{X}_{\mathrm{i,j}}K_G$ to the right hand of eq. S20, we obtain $2\times(Q-2)$ linear equations of the form

$$\mathrm{Y}_{\mathrm{i,j}} \cdot K_{i,j\pm1} + \mathrm{H}_{\mathrm{ij}} \cdot K_{i,j} = \mathrm{G}_{\mathrm{i,j}} - \mathrm{X}_{\mathrm{i,j}} \cdot K_{\mathrm{G}} = \mathrm{G}_{\mathrm{i,j}}. \tag{S25}$$

c) y-edge equations correspond to pixels $(1, j)$ and (P, j) with $j = 2,\ldots, Q-1$ [for which $l = 2,\ldots P-1$ and $l = (Q-1)\times P+2,\ldots,Q\times P-1$ if a single-index notation is used, as in Figure S2]. In these cases, we have $K_{i,j\pm1} = K_G = 0$. By moving the known term $\mathrm{Y}_{\mathrm{i,j}}K_G$ to the right hand of eq. S20, we obtain $2\times(P-2)$ linear equations of the form

$$\mathrm{X}_{\mathrm{i,j}} \cdot K_{i\pm1,j} + \mathrm{H}_{\mathrm{ij}} \cdot K_{i,j} = \mathrm{G}_{\mathrm{i,j}} - \mathrm{Y}_{\mathrm{i,j}} \cdot K_{\mathrm{G}} = \mathrm{G}_{\mathrm{i,j}}. \tag{S26}$$

d) Bulk equations: correspond to pixels that are not situated at the vicinity of the edges. This implies that, in general, each equation of the form S20 presents three nonzero unknowns.

Equations of type S20, in the forms a), b), c) and d), can be combined in a matrix form $\mathbf{A}\cdot K = \mathbf{B}$ that can be solved using sparse-function algorithms (e.g. using Matlab™) so that $\{K_{i,j}\}$ can be determined. By using the compact, single-index notation for which $l = 1, \ldots. P\times Q$ our system $\mathbf{A}\cdot K = \mathbf{B}$ that can be written as

$$\begin{pmatrix} H_{11} & 0 & 0 & 0 & 0 & 0 & 0 & 0 & 0 & 0 \\ -Y_{12} & H_{12} & 0 & 0 & 0 & 0 & 0 & 0 & 0 & 0 \\ 0 & -Y_{13} & H_{13} & 0 & 0 & 0 & 0 & 0 & 0 & 0 \\ 0 & 0 & . & . & 0 & 0 & 0 & 0 & 0 & 0 \\ 0 & 0 & 0 & . & . & 0 & 0 & 0 & 0 & 0 \\ 0 & 0 & 0 & 0 & . & . & 0 & 0 & 0 & 0 \\ -X_{21} & 0 & 0 & 0 & 0 & -Y_{1,P} & H_{1,Q} & 0 & 0 & 0 \\ 0 & -X_{22} & 0 & 0 & 0 & 0 & . & . & 0 & 0 \\ 0 & 0 & . & 0 & 0 & 0 & 0 & . & . & 0 \\ 0 & 0 & 0 & . & 0 & 0 & 0 & 0 & Y_{P,Q-1} & H_{PQ} \end{pmatrix} \cdot \begin{pmatrix} K_{11} \\ K_{21} \\ K_{31} \\ . \\ . \\ . \\ K_{P1} \\ . \\ . \\ K_{PQ} \end{pmatrix} = \begin{pmatrix} G_{11} \\ G_{12} \\ G_{13} \\ . \\ . \\ . \\ G_{P1} \\ . \\ . \\ G_{PQ} \end{pmatrix}. \qquad \text{(S27)}$$

After inverting the equation S27 using a specially designed Matlab™ routine and determining K, the column vector containing the values of (non-calibrated) thermal conductivity per each pixel have been rearranged into a P×Q matrix.

3) Additional images from multifrequency NeSTRI measurements on test sample.

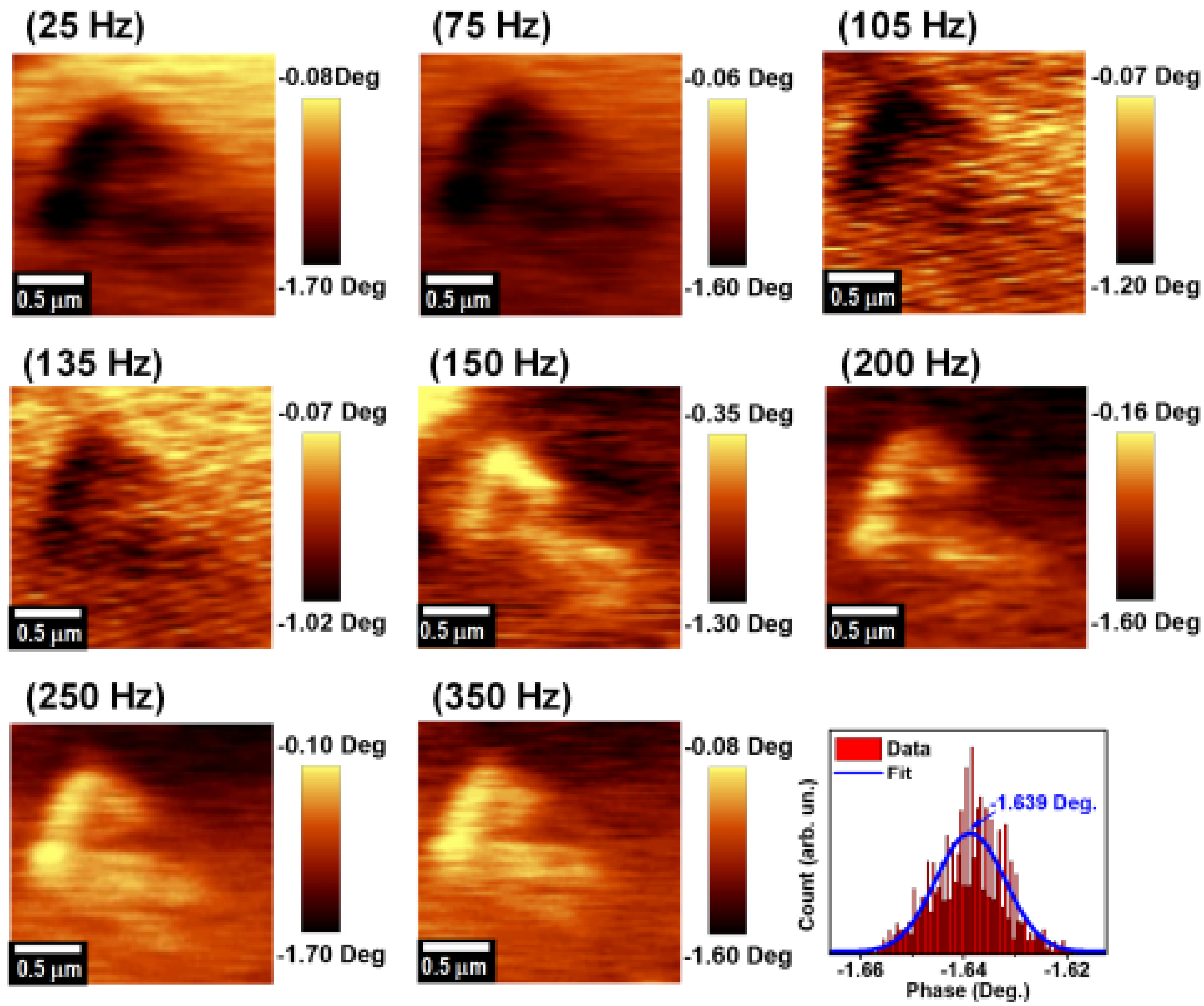

Figure S3. *Multifrequency NeSTRI phase images (measured on test sample as in figure 1b of the paper) and example of fitting procedure on graphene domain. Up to a crossover frequency from 135 Hz to 150 Hz, the phase in the multilayer graphene flake is larger than glass because of long thermal diffusion in graphene limited by the size of graphene. Above the crossover frequency* L_{th} *is controlled by the flake size, and* $L_{th} \sim (D/\omega)^{1/2}$.

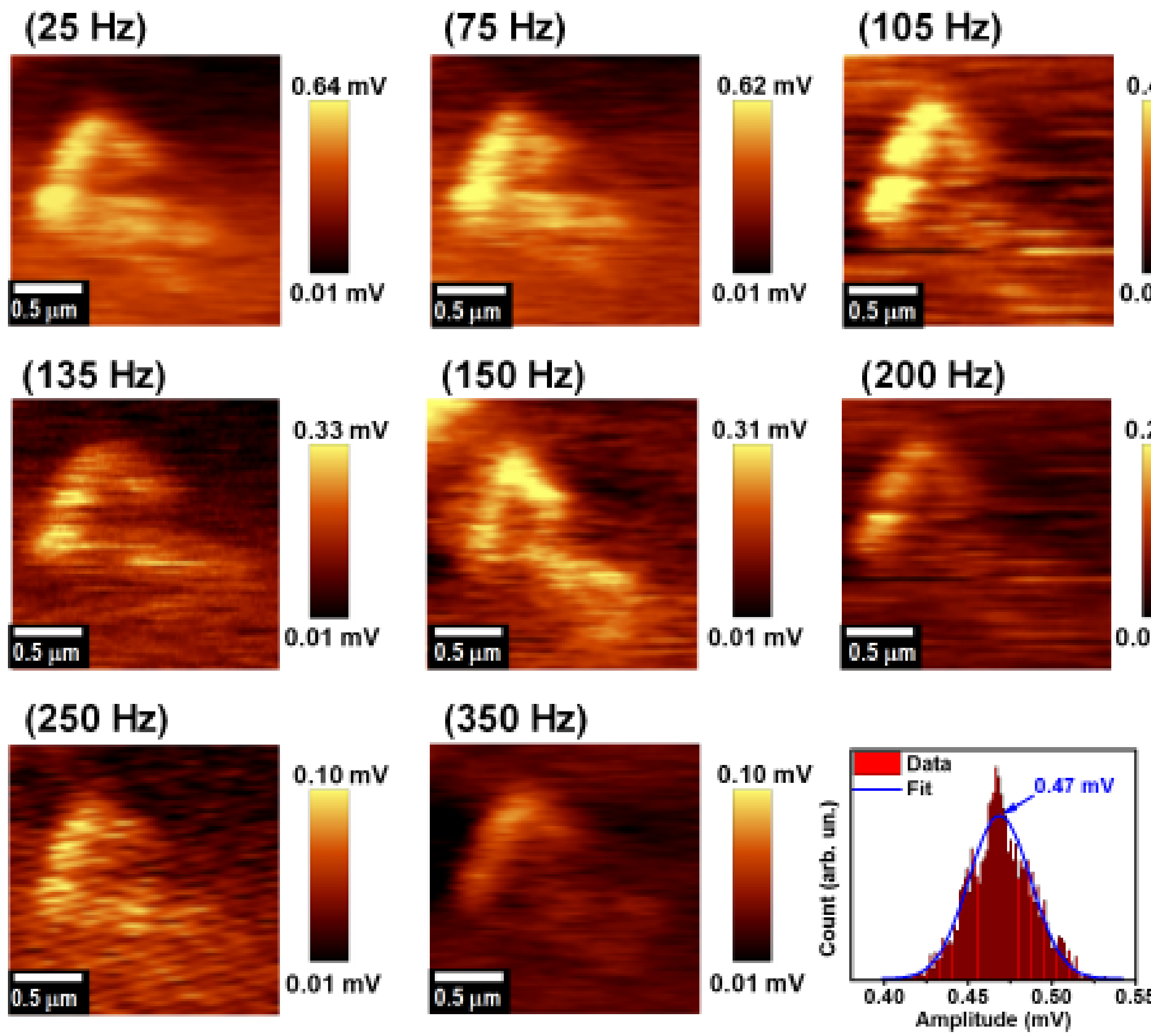

Figure S4. *Multifrequency NeSTRI amplitude images (measured on test sample as in figure 1b of the paper) and example of fitting procedure on graphene domain.*

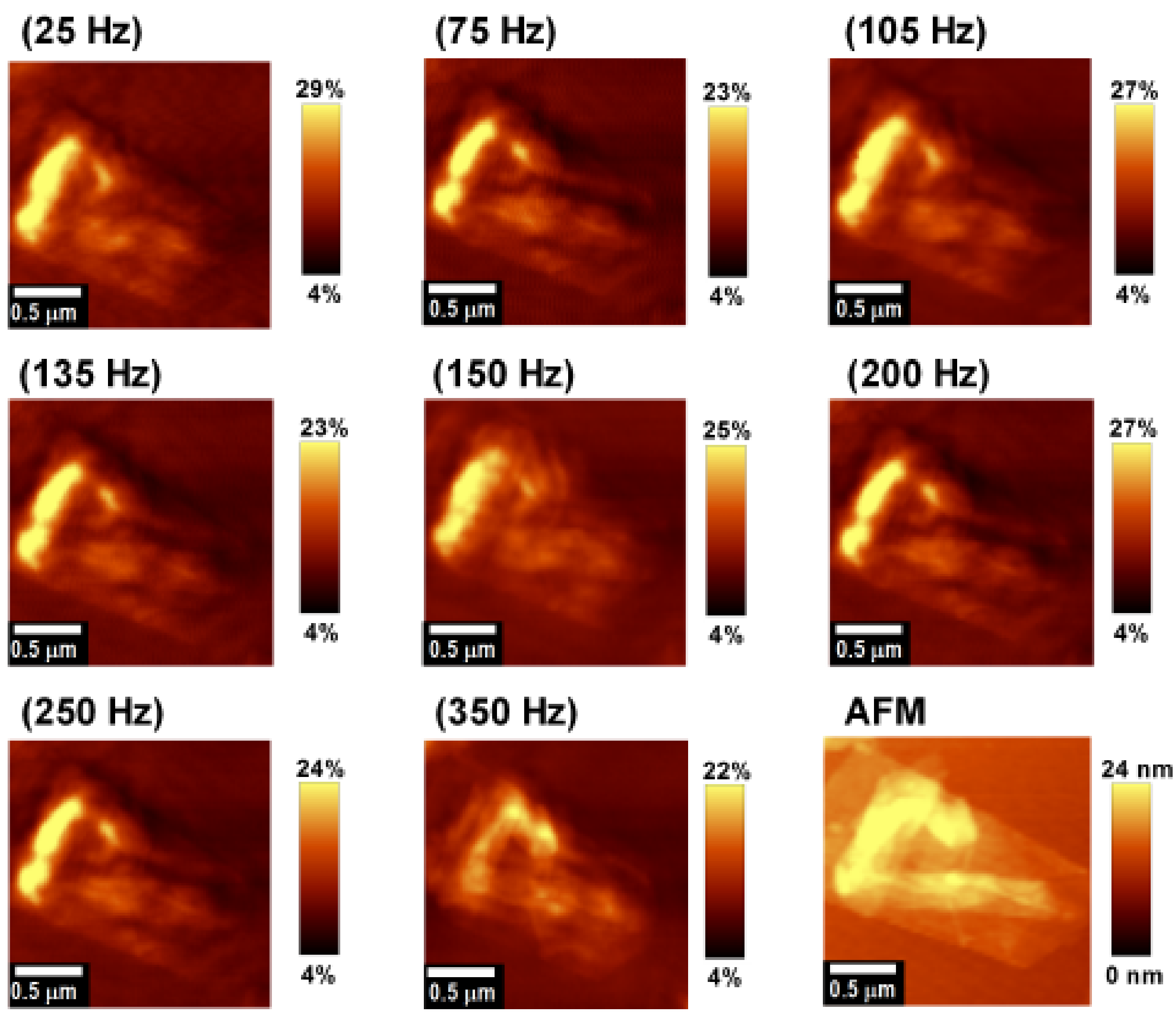

Figure S5. *Continuous wave reflectance images recorded on test sample during NeSTRI measurements (configuration as in figure 1a). Note that the reported frequency values do not indicate that the measurement have been carried out at that specific frequency, but that the reflectance measurement have been carried out immediately after a NeSTRI measurement at the reported frequency, without the lock-in amplifierand with the detector connected to a DC amplifier. The AFM image of the measured graphene domain is also reported.*

4) Negative test measurements

Objective of this section is to demonstrate the genuineness of the amplitude and phase images measured using our experimental apparatus, and show they are originating from thermoreflectance oscillations at the air-sample interface, and not from scanning near-field artefacts, including periodic changes of the tip-surface distance due to periodic thermal expansion of the sample.

To this end, a set of negative test samples, consisting of thermally evaporated aluminum thin films, have been deposited and analyzed. These samples were designed as shown in Figure S6, with a step between a large (several cm^2) and 20-nm thick Al thin film, and an equally large, but thicker (D = 40 nm, 68 nm, or 80 nm), Al film on the right. Samples were prepared by thermal evaporation of Al pellets (K.J. Lesker) in a vacuum chamber integrated to a glovebox operating in nitrogen atmosphere (Nexus II, Vacuum Atmospheres Co.) that is described elsewhere [s7]. A uniform, 20-nm film is initially grown on glass, and the growth rate is checked using a Sycom STM2 quartz crystal monitor. As soon as the desired thickness is reached, a part of the sample is masked, and the deposition continues on the unmasked side of the sample, until the desired thickness D is reached. All samples were measured by NeSTRI, as described in the experimental section of the paper. The presence of a similar, 20-nm thick, region in all of the samples serves as a reference control for the NeSTRI amplitudes, and ensures that measurements performed on different samples are comparable.

Our goal is to demonstrate that all these samples produce NeSTRI images, with amplitudes that are proportional to the volumetric heat that is locally generated within each sample and phases that are independent of the sample thickness. Our negative test samples will ensure that the thermal properties obtained from NeSTRI images do not depend on the sample geometry, but only on the material properties of aluminum. In addition, these experiments are useful to rule out near-field optical artefacts due to periodic thermal dilatation of the samples at the same frequency of the pump beam pulses used for sample heating. If thermal dilatation could not be neglected, it would produce a shift $\delta z(\omega)$ of the sample surface that is proportional to the sample thickness D. A subsequent change of the tip-sample distance, $z_0 - \delta z(\omega)$, will then occur. Consequently, signal amplitudes due thermal dilatation artefacts would be proportional to the film thickness:

$$\delta\rho_0 \propto D. \tag{S28}$$

Conversely, in the case of a genuine NeSTRI signal, the equation of heat (eq. 4) for a uniform thin film region becomes

$$c_{Al}\, dT(t)/dt = H_0 \exp(i\omega t), \tag{S29}$$

where c_{Al} [J/m^3/K] is the volumetric specific heat of Al and H_0 [W/m^3], the heat generated per unit volume of the sample, corresponds to the amount of light being absorbed by the entire cross section of an Al thin film at the pump-beam wavelength of 405 nm:

$$H_0 = (P_0/D^2) \int_0^D \exp(-\alpha_{Al} z)\, dz = [P_0/(\alpha_{Al} D^2)][1 - \exp(-\alpha_{Al} D)], \tag{S30}$$

Where P_0 [in W/m^2] is the photon flux of the pump beam, and $\alpha_{Al} = 1.5\ 10^8$ m^{-1} is the optical absorption coefficient of Al at 405 nm, the pump beam wavelength [s6]. As discussed in the text, a tentative uniform solution of the form

$$\delta\rho(t) = -hT(t) = -hT_0 \exp[i(\omega t - \delta\varphi_0)] = \delta\rho_0 \exp[i(\omega t - \delta\varphi_0)] \tag{S31}$$

can be sought and replaced into eq. S29. In eq. S31, h is a proportionality coefficient (see Supplementary Information Section 1) and $\delta\rho(t)$ is the oscillatory thermoreflectance signal of amplitude $\delta\rho_0$ and phase $\delta\varphi_0$, caused by temperature oscillations of amplitude T_0. By replacing eqs. S30 and S31 into eq. S29, we then obtain

$$\delta\rho_0 = hP_0/(\omega c_{Al} \alpha_{Al} D^2)[1 - \exp(-\alpha_{Al} D)]$$

$$\delta\varphi_0 = -90^0 = \mathrm{const}(D). \tag{S32}$$

Contrarily to eq. S28, eq. S32 indicates that genuine NeSTRI amplitude signals decrease at increasing thickness because of lower power density generated in thicker and more voluminous samples, which produce smaller temperature raises. This can be appreciated from figure S6, which shows that the left (20-nm thick) side of the image of $\delta\rho_0$ exhibits a significantly higher amplitude of the right side (40-nm thick) of the image. Conversely, the image of $\delta\varphi_0$ does not exhibit any significant difference or thickness dependence far away from the interface between the two thicknesses. Since eq. S32 indicates that $\delta\rho_0$ does not depend on the thermal conductivity k in a homogeneous and flat region, but only on the volumetric specific heat c, the information on k contained in $\delta\varphi_0(x, y)$, for values of x within a few thermal diffusion lengths in the proximity of an edge, are critical to determine k in uniform thin films by NeSTRI.

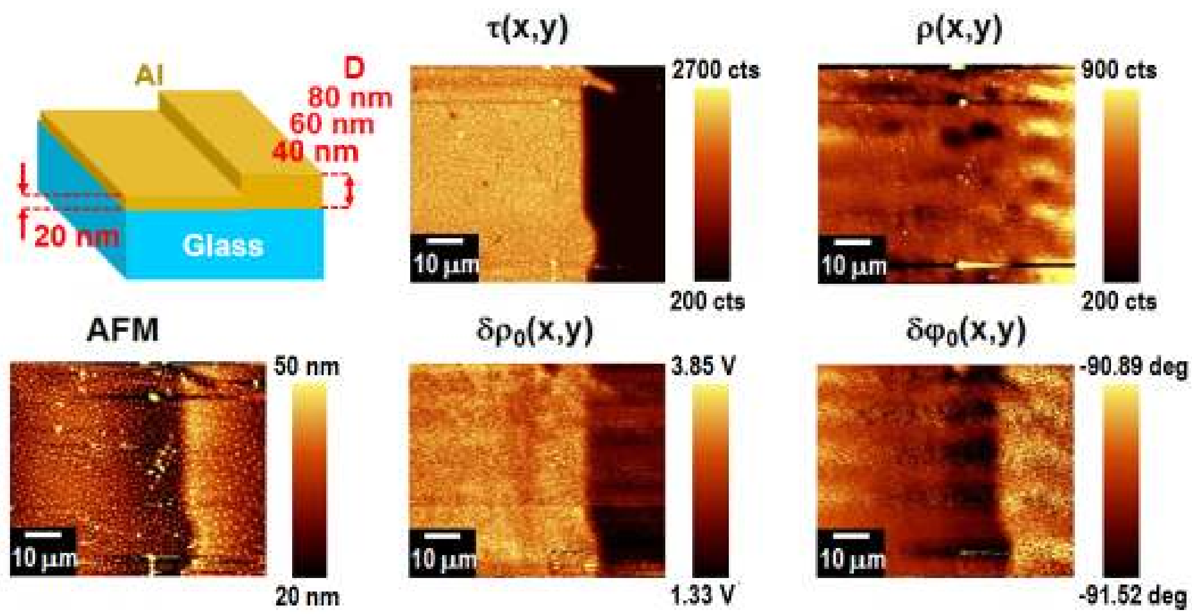

Figure S6. *Geometry of negative test samples, with corresponding 405-nm SNOM images in transmittance* (τ) *and reflectance* (ρ)*. AFM shows that images are taken at the edge between 20-nm thick and 40-nm thick Al regions. The granular structures of aluminum present on both regions are not visible in the thermal images, of which the phase* ($\delta\varphi_0$) *becomes thickness-independent at ~30 µm from the edge, while the amplitude* ($\delta\rho_0$) *decreases with thickness accordingly to eq. S32.*

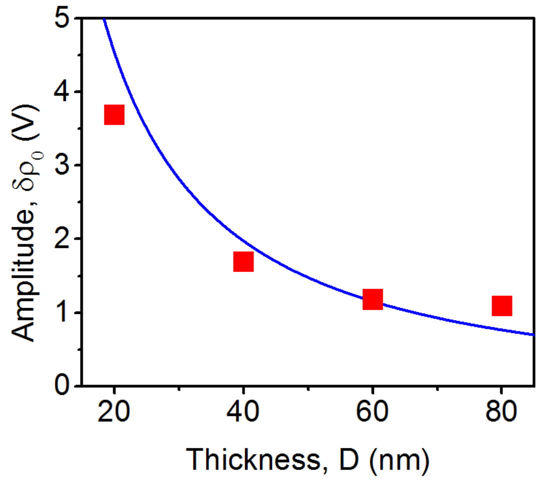

Figure S7. *NeSTRI signal amplitude* ($\delta\rho_0$) *as a function of Al thin film thickness* (D). *The blue line is a data fitting accordingly to eq. S32. The fact that* $\delta\rho_0$ *decreases at increasing* D*, as well as the good quality of the fit, are a strong indication of the genuineness of the NeSTRI signal, originated from thermoreflectance effects at the air-sample surface. Conversely, near-field optical artefacts would have led* $\delta\rho_0$ *to increase proportionally to the thin-film volume per unit surface area and, consequently, with* D.

The findings presented in Figure S6 are quantified and further substantiated in Figure S7 that reports the NeSTRI signal amplitude as a function of Al thickness for the entire set of negative test samples. The blue line in Figure S6 is a data fitting accordingly to eq. S32. The fitting quality is remarkably good, which is an additional strong indication that the NeSTRI signal originates from thermoreflectance effects at the air-sample surface, and not from thermal expansion artefacts that would have led the amplitude of the signal to linearly increase with D. Finally, from Figure S6, it is apparent that the granular Al structures that can be observed in the AFM image are also reproduced in the reflection (ρ) and transmission (τ) SNOM images, but do not significantly affect the NeSTRI images, neither in phase nor amplitude. We can thus infer that NeSTRI is free from nano-optical artifacts [s8] producing images that are mere optical readouts of the AFM topography.

References

[s1] J. D. Jackson, Classical Electrodynamics (3rd ed.) New York, John Wiley & Sons.

[s2] C. F. Bohren and D. R. Huffman, Absorption and Scattering of Light by Small Particles, New York, Wiley-VCH Verlag & Co.

[s3] N. Ashcroft and N. D. Mermin, *Solid State Physics*, Saunders College, Philadelphia, 1976

[s4] S.E. Bialkowski, Photothermal Methods for Chemical Analysis, New York, Wiley, 1996.

[s5] G. Langer, J. Hartmann and M. Reichling, Rev. Sci. Instr. (1997) 68, 1510

[s6] A.D. Rakić, A.B. Djurišic, J.M. Elazar, and M.L. Majewski. Appl. Opt. (1998) 37, 5271 - See also http://refractiveindex.info database (consulted: Feb-14-2017).

[s7] S. Ezugwu, MSc Thesis, The University of Western Ontario (2012) – Available online at http://ir.lib.uwo.ca/etd/1025/ (consulted: Feb-14-2017).

[s8] P.G. Gucciardi and M. Colocci, Appl. Phys. Lett. (2001) 79, 1543-1545.